7-2014

Measuring Tumor Cycling Hypoxia and Angiogenesis Using a Side-firing Fiber Optic Probe

Bing Yu
Marquette University, bing.yu@marquette.edu

Amy Shah
Duke University

Bingqing Wang
Duke University

Narasimhan Rajaram
Duke University

Quanli Wang
Duke University

See next page for additional authors

Journal of Biophotonics, Vol. 7, No. 7 (July 2014): 552-564. DOI.

Measuring Tumor Cycling Hypoxia and Angiogenesis Using a Side-firing Fiber Optic Probe

Bing Yu
Department of Biomedical Engineering, The University of Akron, Akron, OH
Department of Biomedical Engineering, Duke University, Durham, NC
Amy Shah
Department of Biomedical Engineering, Duke University, Durham, NC
Bingqing Wang
Department of Biomedical Engineering, Duke University, Durham, NC
Narasimhan Rajaram
Department of Biomedical Engineering, Duke University, Durham, NC
Quanli Wang
Department of Statistical Science, Duke University, Durham, NC
Nirmala Ramanujam
Department of Biomedical Engineering, Duke University, Durham, NC

Gregory M. Palmer
Department of Radiation Oncology, Duke University, Durham, NC
Mark W. Dewhirst
Department of Biomedical Engineering, Duke University, Durham, NC
Department of Radiation Oncology, Duke University, Durham, NC

Abstract

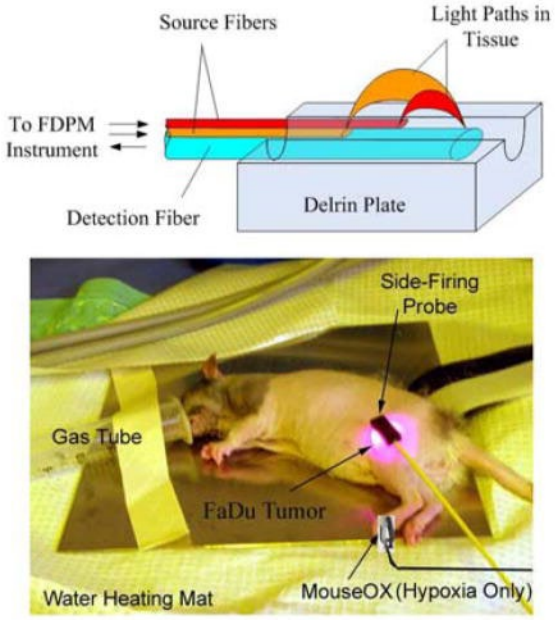

Hypoxia and angiogenesis can significantly influence the efficacy of cancer therapy and the behavior of surviving tumor cells. There is a growing demand for technologies to measure tumor hypoxia and angiogenesis temporally *in vivo* to enable advances in drug development and optimization. This paper reports the use of frequency-domain photon migration with a side-firing probe to quantify tumor oxygenation and hemoglobin concentrations in nude rats bearing human head/neck tumors administered with carbogen gas, cycling hypoxic gas or just room air. Significant increase (with carbogen gas breathing) or decrease (with hypoxic gas breathing) in tumor oxygenation was observed. The trend in tumor oxygenation during forced cycling hypoxia (CH) followed that of the blood oxygenation measured with a pulse oximeter. Natural CH was also observed in rats under room air. The studies demonstrated the potential of the technology for longitudinal monitoring of tumor CH during tumor growth or in response to therapy.

A flat side-firing fiber optic probe based on frequency-domain photon migration can be easily and reliably attached to a tumor surface for longitudinal monitoring of tumor cycling hypoxia and angiogenesis.

Keywords
Diffuse optical spectroscopy, fiber optic sensor, tumor hypoxia and angiogenesis, cancer therapy

1. Introduction
Hypoxia and angiogenesis are two important characteristics of growing human tumors. Tumor hypoxia or low oxygen status is a spatially and temporally heterogeneous phenomenon, and is influenced by both the oxygen

consumption rate of tumor cells and the oxygen supply from blood vessels [1, 2]. Proliferating cells have an oxygen consumption rate that is 3–5 times greater than that of inactive cells [3–5]. Limited oxygen supply to the tumor can be caused by low vascular density, abnormal vascular orientation, or a paucity of arterial supply vessels [2]. Hypoxia generates a stress response which signals the tumor cells to stimulate blood vessel growth or angiogenesis to provide rapidly proliferating tumor cells with an adequate supply of oxygen and metabolites [2, 6, 7]. The blood vessels in tumors grow much more rapidly than the normal blood vessels, but they are abnormal and leaky, further perpetuating tumor hypoxia.

In a fast growing tumor oxygen diffuses a distance of 100–150 μm from blood vessels which divides a tumor into two different hypoxic regions [8, 9]. Tumor cells beyond the diffusion distance become chronically hypoxic due to poor oxygen supply. Within the diffusion limit, however, tumor oxygenation often shows a temporal fluctuation with clear patterns of periodicity across many tumor types, a phenomenon known as cycling hypoxia (CH) or intermittent (or acute) hypoxia [2, 7–12]. CH has been found in both animal and human solid tumors. Depending on the architectural complexity and maturation level of the tumor vascular network, the periodicity of tumor CH can range between tens of seconds to hours, or even days and varies across tumors and also within the same tumor [2, 11, 12]. The higher frequency (tens of seconds – hours) is associated with changes in perfusion, red blood cell flux, and occasionally vascular occlusion, while the lower frequency (days) is believed to be caused by changes in vascular network structures as a consequence of vascular reformation and angiogenesis [8, 12].

Tumor angiogenesis and hypoxia, particularly CH, can significantly influence the efficacy of radiotherapy and chemotherapy as well as the behavior of surviving cancer cells. Angiogenesis and hypoxia are inextricably linked to the propensity of a tumor to grow. It is well known that hypoxia leads to neovascularization in order to satisfy the increased need of proliferating tumor cells, enhanced tumor metastasis, and resistance to radiation and chemotherapy by increasing genetic instability and selecting for cells with a diminished apoptotic potential [8, 13, 14]. It has been recently demonstrated that CH also increases tumor angiogenesis by increasing hypoxia-inducible factor 1α (HIF-1α stabilization and HIF-1 activation [7, 15] and confers tumor cells and tumor vascular endothelial cells with enhanced pro-survival pathways, making tumors less responsive to radiation and chemotherapy. However the dynamic interplay between hypoxia and angiogenesis and how best to leverage these targets for cancer therapy is still the subject of numerous investigations. Hypoxia-directed intensity-modulated radiotherapy and anti-angiogenic therapy in combination with cytotoxic chemotherapy are examples of current approaches that are being explored to target tumor hypoxia and/or angiogenesis in various tumor entities [16, 17]. There is growing demand for technologies to measure tumor hypoxia and angiogenesis temporally *in vivo* to enable advances in drug screening, development and optimization.

Pre-clinical tumor models are important test beds in the development of drug therapies because they allow for rapid and systematic evaluation of different combinations of therapy and doses as well as the sequence in which they are administered in a relatively fast and cost-effective manner before proceeding to expensive, time-consuming clinical trials. However, the insights gained from pre-clinical model studies are only as effective as the tools used to measure the relevant endpoints. Sophisticated imaging techniques such as electron paramagnetic resonance imaging (EPRI), positron-emission tomography (PET), magnetic resonance imaging (MRI), fluorescence redox imaging and photoacoustic imaging can be used to image tumor hypoxia and angiogenesis with a spatial resolution from several millimeters down to a few micrometers [12, 18]. However, these tools are not amenable to frequent use and thus at best can only report on events at selected time points over the course of cancer therapy. Moreover, multiple types of sophisticated imaging modalities maybe needed to fully capture events related to tumor hypoxia and angiogenesis. These tools could miss opportunistic time points and/or the interaction between key bio-markers that report on the effect of a particular drug. Needle-based oxygen electrodes and fluorescence oxygen sensors have also been widely used in the past, but these techniques are

invasive, sample a very small volume, and have short lifetime. Immunohistochemistry of tissue biopsies suffers from similar drawbacks, in addition to the fact that biopsies are invasive and sample only very small volumes of tumor, which may not represent the overall tumor behavior.

Frequency-domain photon migration (FDPM) or diffuse optical spectroscopy (DOS) is a noninvasive technology that can provide quantitative information about tumor physiology, including tissue hemoglobin content and oxygenation status [19–27]. We previously reported a three-wavelength FDPM instrument and a side-firing fiber optic probe as an adjunct tool for breast cancer detection during image guided core-needle biopsy [28]. We have recently upgraded the instrument and redesigned a completely flat side-firing probe. The new system can quantitatively measure bulk tissue absorption and scattering spectra between 650–1000 nm with a penetration depth between 5–15 mm within human tissue. The concentrations of deoxyhemoglobin (Hb) and oxyhemoglobin ($\mathrm{HbO_2}$) can be determined from the absorption spectra. The side-firing probe can be easily and reliably attached to a flat skin surface, making it an ideal tool for continuous monitoring of tumor physiology in preclinical tumor models. In this paper, we report the use of the side-firing probe in a preclinical model for longitudinal monitoring of head & neck (FaDu) tumor physiology in response to high or low oxygen levels or just room air. The tissue oxygen saturation measured via side-firing probe accurately tracked the varying oxygenation status of the tumor and was concordant with arterial blood oxygen saturation measured with a mouse pulse oximeter. Natural CH with patterns and frequency range similar to those reported in literature was also recorded in some rats under room air. To the best of our knowledge, this is the first time natural tumor CH was observed in animal models using a noninvasive optical technique.

2. Materials and methods

2.1 Instrument

In this study, the FDPM instrument was upgraded to include 6 laser wavelengths (654, 683, 779, 805, 847, and 905 nm) so that more absorbers, such as water and fat, can be accounted for. Figure 1(a) shows a photograph of the 6-wavelength FDPM instrument. The needle-shaped side-firing fiber optic probe used in the previous breast biopsy study was modified to have a completely flat surface by gluing all fiber tips into a V-groove on a thin Delrin plate so that it could be easily attached on to the surface of a rat tumor, shown in Figures 1(b) and (c). The probe has two side-firing source fibers (200/220/240 μm, NA = 0.22) and a single side-firing detection fiber (600/660/710 μm, NA = 0.22), providing two source-detector separations (SDS) of 5 and 10 mm, respectively. The fiber tips were polished to a 45° angle and coated with a mirror to create a light path perpendicular to the fiber. The two source-detector separations were used to eliminate instrumentation artifacts due to modulation-dependence of the light sources and instrument response [29, 30] and skin effects. The fibers were relayed to the instrument via a 2.5 mm fiber optic cable with FC connectors. The FDPM instrument launches intensity-modulated continuous wave lasers into the tissue and collects the amplitude-attenuated and phase-shifted diffuse reflectance from the tissue at the same frequency of the incident light. The optical switch outputs each of the six wavelengths to one of two source fibers sequentially and the modulation frequency was scanned from 50 to 250 MHz at a 1 MHz interval at each wavelength. A custom LabVIEW program integrated with Matlab scripts was used for instrument control, data acquisition and data analysis. The measured tissue optical properties as well as composition parameters were displayed in real-time.

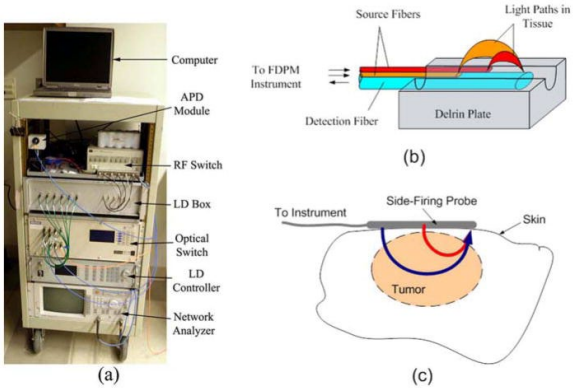

Figure 1 FDPM instrument and side-firing probe: (**a**) photograph of the instrument; (**b**) a schematic of the side-firing fiber optic probe; and (**c**) a cartoon of the coupling between the side-firing probe and rat tumor.

2.2 Phantom study

Tissue-simulating liquid phantoms were used to evaluate the performance of the system and for instrument calibration. 15 phantoms with absorption (μ_a) and reduced scattering coefficients (μ_s') representative of rat tumors at the six wavelengths [21, 31] were created by fixing the number of scatterers (or volume of 20% stock Intralipid solution) at three levels (low, medium and high) and titrating stock India ink solution (absorber) to five levels. The extinction coefficient of the stock ink solution was measured using a spectrophotometer (Cary 300, Varian, Inc.) and the expected μ_s' of the stock Intralipid was determined by using the method described in Ref. [32]. Table 1 summarizes the expected phantom μ_a and μ_s' averaged over all the six wavelengths.

Table 1 Expected phantom μ_a and μ_s' averaged over all six wavelengths.

Phantom #	$\boldsymbol{\mu_a}$ **(cm^{-1})**	μ_s' (cm−1)	**Phantom #**	$\boldsymbol{\mu_a}$ **(cm^{-1})**	μ_s' (cm−1)
1	0.108	10.63	9	0.305	14.01
2	0.162	10.60	10	0.376	13.99
3	0.234	10.55	11	0.108	17.71
4	0.305	10.51	12	0.162	17.66
5	0.376	10.47	13	0.234	17.59
6	0.108	14.17	14	0.305	17.52
7	0.162	14.12	15	0.376	17.45
8	0.234	14.07			

2.3 Animal tumor models

A human head & neck tumor model (FaDu) in athymic nude rats (Charles River, Durham, North Carolina) was used for the study. A total number of 26 rats (200–240 g) were used in the experiments and the animals were divided into three groups. 8 tumor-bearing rats were assigned to Group 1 and exposed to carbogen gas (95% O_2 and 5% CO_2) for the duration of the experiment. Group 2 had 10 tumor-bearing and 4 control (tumor-free) rats for the forced CH experiment. Finally, 4 rats were assigned to Group 3 and used to study natural CH. The study was approved by the Duke Institutional Animal Care and Use Committee.

To grow the FaDu tumor, about 5 million FaDu cells were injected into the left flank of the rat. The tumors were allowed to grow to a size of ~2.0 cm in diameter (in 3–4 weeks). In each experiment, the side-firing probe was placed on the surface of the tumor or flank muscles (controls) during the study, as shown in Figure 2. The probe has an estimated sensing depth of 5–15 mm. A piece of medical dark tape was used to hold the probe in place

and prevent the room light from saturating the avalanche photodiode (APD) detector. At the end of the experiment the rat was sacrificed using an overdose of Pentobarbital.

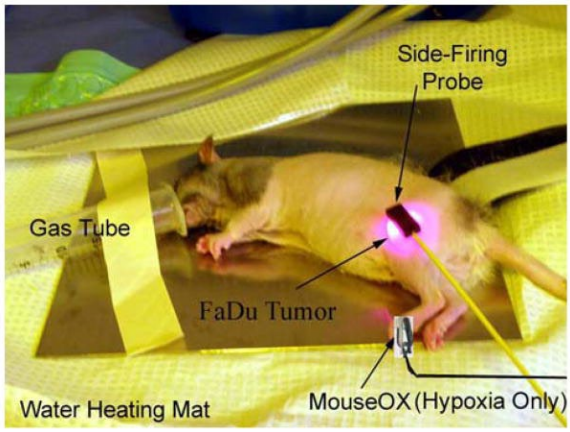

Figure 2 Photograph of a rat with a side-firing probe attached.

2.3.1 Carbogen inhalation experiment

In the first experiment, 8 nude rats (Group 1) bearing a FaDu tumor underwent carbogen inhalation. The rats were subject to measurements when the tumors reached a size of approximately 2 cm × 2 cm. The animals were anesthetized with Pentobarbital at a dose of 50 mg/kg. The experimental procedure is depicted in Figure 3(a). The rats were first exposed to room air for 10 minutes as a baseline (or normoxia), followed by carbogen gas (hyperoxia) through a nosecone for 15 minutes and 20 minutes of room air for recovery. Optical measurements were taken at one-minute intervals resulting in a total of 45 data points for each animal.

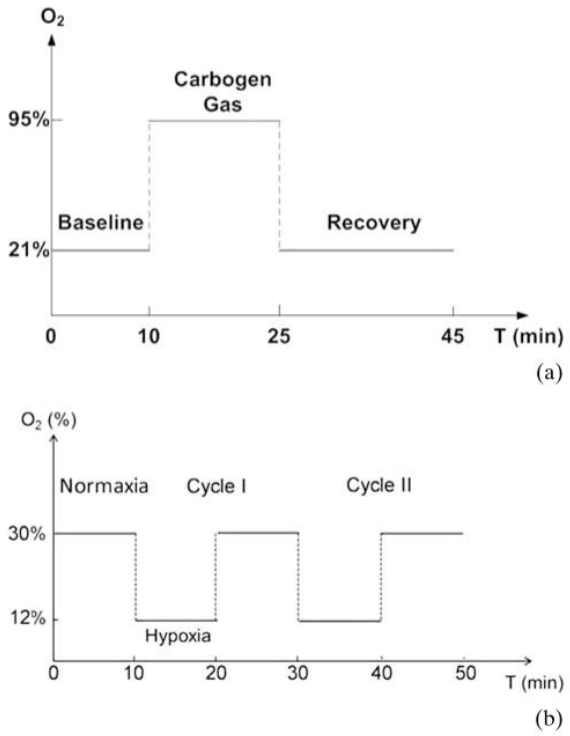

Figure 3 Experimental procedures for (**a**) carbogen (95% O_2 and 5% CO_2) inhalation and (**b**) for cycling hypoxic gas breathing (30% O_2 was used for normoxia instead of 21%).

2.3.2 Forced CH

In the second experiment, 10 tumor bearing rats and 4 normal controls (Group 2) were provided with cycling hypoxic gas following the procedure outlined in Figure 3(b). The experiments were conducted when tumors were approximately 2 cm × 2 cm. The animals were anesthetized with Pentobarbital at a dose of 50 mg/kg. The rats were first provided normoxic gas (30% O_2 and 70 N_2) for 10 minutes as a baseline, followed by hypoxic gas (mixture of 12% O_2 and 88% N_2) for 10 minutes. The procedure was repeated for two cycles. Finally, the rats were provided with normoxic gas again for another 10 minutes to follow recovery. Because Pentobarbital injection was used for anesthesia, the oxygen concentration for the normoxia phases was slightly raised from the natural level of 21% to 30% to better simulate a natural normoxic condition. An optical measurement was taken every minute, resulting in a total of 50 data points. A mouse pulse oximeter (Mouse Ox, Starr Life Science Corp., Allison Park, PA) was also clamped on to the left foot of the rat and the arterial blood oxygen saturation was collected every 5 seconds as a reference as well as for rat condition monitoring.

2.3.3 Natural CH

To evaluate the capability of the side-firing probe in capturing natural CH, a much weaker signal comparing to the forced CH, 4 nude rats (Group 3) bearing a FaDu tumor were used to investigate the capability of the side-firing probe in quantifying and continuous monitoring natural tumor CH. The animals were anesthetized with a mixture of vaporized Isofluorane and fresh air under a fume hood during the experiment. The first 2 animals (Group 3A) were measured on two different days: Day 1 – before tumor cells were injected and Day 2 – when the tumor size reached approximately 2 cm in diameter (3–4 weeks later). The 2 remaining rats (Group 3B) were measured on three different days: Day 1 – before tumor cells were injected, Day 2 – when the tumor size reached approximately 0.5 cm in diameter, and Day 3 – when the tumor size reached approximately 1.5 cm in diameter. On each day optical measurements were taken from each animal at one-minute intervals for about 120–150 minutes. The purpose was to study the relationship between CH and tumor size.

2.4 Data analysis

In frequency-domain photon migration, the AC component of the amplitude AC (*r, λ, ω)* and phase-shift *Φ(r, λ, ω)* of the diffuse reflectance of the photon density wave collected by the detection fiber from the surface of a semi-infinite medium at SDS = *r* can be expressed by the following equations that were modified from Eqs. (8)–(13) in Ref. [20]:

$$\mathrm{AC}\ (r,\ \lambda,\ \omega)\ =\ (A_0/4\pi\ D)\ (\mathrm{REAL}^2 + \mathrm{IMAG}^2)^{1/2} \tag{1}$$

$$\phi(r,\ \lambda,\ \omega)\ =\ \phi_0\ +\ k_{\mathrm{imag}}(\omega)\ r_0\ -\ \arctan\ (\mathrm{IMAG/REAL}) \tag{2}$$

where,

$$\mathrm{REAL}\ =\ \exp[-k_{\mathrm{real}(\omega)}r_0]/r_0\ \ -\ \cos\left[k_{\mathrm{imag}}(\omega)\ (r_{0b}\ -\ r_0)\right]\ \times\ \exp[-k_{\mathrm{real}}(\omega)r_{0b}]/r_{0b} \tag{3}$$

$$\mathrm{IMAG}\ =\ \sin\left[k_{\mathrm{imag}}(\omega)\ (r_{0b}\ -\ r_0)\right]\ \exp[-k_{\mathrm{real}}(\omega)r_{0b}]/r_{0b} \tag{4}$$

$$r_0 = [(1/\mu_s')^2 + r^2]^{1/2}$$

(5)

$$r_{0b} = \{[4(1 + R_{\text{eff}})/3\mu_s'(1 - R_{\text{eff}})]^2 + r^2\}^{1/2}$$

(6)

$$k_{\text{real}} = \sqrt{3\mu_a\mu_s'/2}\{[1 + (\omega/\nu\mu_a)^2]^{1/2} + 1\}^{1/2}$$

(7)

$$k_{\text{real}} = \sqrt{3\mu_a\mu_s'/2}\{[1 + (\omega/\nu\mu_a)^2]^{1/2} + 1\}^{1/2}$$

(8)

$$D = 1/3(\mu_a + \mu_s')$$

(9)

and A_0 is the net amplitude response of the instrument, ϕ_0 is the initial phase shift due to the cables and electronics, R_{eff} is an effective reflection coefficient ($R_{\text{eff}} = 0.431$ for air-water and 0.493 for air-tissue interfaces), ν is the velocity of light in the medium, and $\omega = 2\pi f$ is the angular modulation frequency, where f is the modulation radio frequency. The major modification is that an initial phase shift ϕ_0 due to cables and electronics compared with that of the local reference RF signal is added to the total phase.

Assuming that the two source fibers had identical signal attenuation and initial phase delay, the relative amplitude attenuation ($\Delta\text{AC}(\lambda, \omega)$) was obtained by dividing the amplitude of the long SDS (r_2) by that of the short SDS (r_1) and the relative phase-shift ($\Delta\Phi(\lambda, \omega)$) was calculated as the difference between the phases of the two SDSs:

$$\Delta\text{AC}(\lambda, \omega) = \text{AC}(r_2, \lambda, \omega)/\text{AC}(r_1, \lambda, \omega)$$
$$= \{[\text{REAL}(r_2, \lambda, \omega)^2 + \text{IMAG}(r_2, \lambda, \omega)^2]/[\text{REAL}(r_1, \lambda, \omega)^2 + \text{IMAG}(r_1, \lambda, \omega)^2]\}^{1/2}$$

(10)

$$\Delta\phi(\lambda, \omega) = \phi(r_2, \lambda, \omega) - \phi(r_1, \lambda, \omega)$$
$$= k_{\text{imag}}(\lambda, \omega)[r_0(r_2, \lambda) - r_0(r_1, \lambda)] - \arctan[\text{IMAG}(r_2, \lambda, \omega)/\text{REAL}(r_2, \lambda, \omega)] +$$
$$arctan[\text{IMAG}(r_1, \lambda, \omega)/\text{REAL}(r_1, \lambda, \omega)]$$

(11)

By using two source-detector separations, the source term A_0 and initial phase shift ϕ_0 can be removed, which makes the system insensitive to the absolute instrument throughput and phase shift as well as fluctuations. The relative attenuation and the phase-shift of these photon density waves in a semi-finite medium are determined by three wave characteristics, the modulation frequency f, the source-detector separations (r_1 and r_2), and the medium characteristics (μ_a and μ_s').

The tissue or phantom optical properties $\mu_s'(\lambda)$ at each wavelength λi were independently extracted by fitting the measured relative diffuse reflectance data to the theoretical model based on Eqs. (3)–(11). The data analysis algorithm was implemented by a MATLAB (MathWorks, Inc., Natick, MA) script node in LabVIEW (National Instruments Corp., Austin, TX). A Levenberg-Marquardt nonlinear least square minimization algorithm was adapted to simultaneously fit the relative amplitude $\Delta\text{AC}(\lambda, \omega)$ with a weight α and phase-shift $\Delta\Phi(\lambda, \omega)$ with a weight $(1 - \alpha)$. An optimal $\alpha = 0.8$ has been used for both the phantom and animal studies described in

this paper. Various initial guesses of $\{\mu_{a0}(\lambda),\ \mu_s'(\lambda),\ \alpha_0\}$ were used to guarantee that the chi-squared value (goodness-of-fit metric) was at the global minimum.

To account for the difference between the theoretical model and experimental data and difference in the attenuation and optical path length of the two source fibers, the relative amplitude and phase shift obtained from one or multiple reference phantoms were fit to the diffusion model to generate three correction factor matrices: an amplitude multiplication factor $X(\lambda_i)$, an amplitude offset factor $Y(\lambda_i)$ and a frequency-dependent phase offset factor $Z(\lambda_i,\ f)$ as given by:

$$\Delta\mathrm{AC}_{\mathrm{theoretical}}\,(\lambda_i)\ =\ X(\lambda_i)\ \cdot\ \Delta\mathrm{AC}_{\mathrm{ref\_phantom}}\,(\lambda_a)\ +\ Y(\lambda_i)$$

(12)

$$\Delta\phi_{\mathrm{theoretical}}(\lambda_i,\ f)\ =\ \Delta\phi_{\mathrm{ref\_phantom}}(\lambda_i,\ f)\ +\ Z(\lambda_i,\ f)$$

(13)

The correction factors were then applied to the relative amplitude and phase shift measured from the animals before the nonlinear least square fitting.

Next, tissue physiological parameters, including $\mathrm{HbO_2}$ concentration $\mathrm{C_{HbO_2}}$, Hb concentration $\mathrm{C_{Hb}}$, total hemoglobin concentration (THb) and tissue oxygenation ($\mathrm{SO_2}$) were calculated from the absorption coefficients that were extracted from the tissue spectra, using the Eqs. (14)–(16):

$$\mu_a(\lambda_i)\ =\ 2.303\ \cdot\ [\varepsilon_{(\mathrm{HbO_2},\lambda_i)}\mathrm{C_{HbO_2}}\ +\ \varepsilon_{(\mathrm{Hb},\lambda_i)}\mathrm{C_{Hb}}]$$

(14)

$$\mathrm{THb}\ =\ \mathrm{C_{HbO_2}}\ +\ \mathrm{C_{Hb}}$$

(15)

$$\mathrm{SO_2}\ =\ \mathrm{C_{HbO_2}}/\mathrm{THb}$$

(16)

where $\varepsilon_{(\mathrm{HbO_2},\lambda_i)}$ and $\varepsilon_{(\mathrm{Hb},\lambda_i)}$ are the extinction coefficients of $\mathrm{HbO_2}$ and Hb, respectively.

In both the carbogen inhalation and forced CH experiments, one-way repeated measures ANOVA was employed to examine if there is statistically significant difference between the tissue physiological parameters ($\mathrm{SO_2}$ and THb) under different oxygen supply levels.

3. Results

3.1 Phantom study

The diffuse reflectance spectra measured from 15 Intralipid phantoms were analyzed using Eqs. (3)–(13) at each wavelength. Figure 4(a) shows the raw, calibrated and expected (modeled) ΔAC and ΔΦ between 50–250 MHz at 654 nm for phantoms #1, 8 and 15 with low, medium and high (μ_a, μ_s'), respectively. Using a modulation frequency depend calibration factor $Z(\lambda_i,\ f)$ significantly improved the fits between the experimental and modeled phase spectra $\Delta\Phi(\lambda,\ \omega)$ compared with calibration with a frequency-independent phase offset factor $Z(\lambda_i)$ that was used in the previous biopsy study [28]. The calibrated relative amplitude and phase shift were used to extract the phantom μ_a and μ_s' at all wavelengths. Figure 4(b) is a scattered plot of the extracted

vs. expected phantom μ_a and μ_s' at all the 6 wavelengths for all 15 phantoms. The errors for μ_a and μ_s' extraction are 9.4 ± 2.8% and 3.4 ± 1.4% with frequency dependent phase calibration, and 14.6 ± 7.7% and 7.3 ± 1.4% with frequency independent phase calibration, respectively.

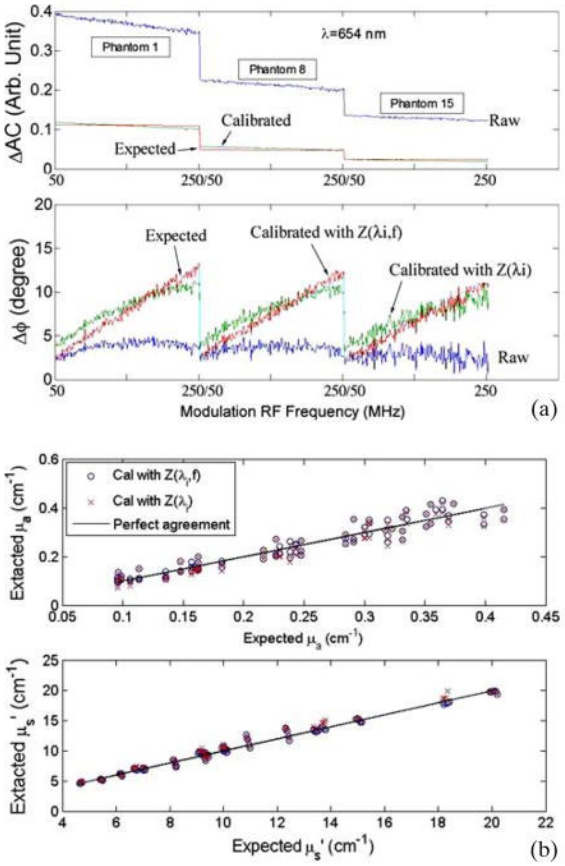

Figure 4 Phantom results: (**a**) Raw and calibrated relative amplitude and phase spectra (in frequency domain) for phantoms #1, 8 and 15. (**b**) Extracted v.s. expected μ_a and μ_s' at all wavelengths for all phantoms. The errors for μ_a and μ_s' extraction are 9.4 ± 2.8% and 3.4 ± 1.4% with frequency dependent phase calibration and 14.6 ± 7.7% and 7.3 ± 1.4% with frequency independent phase calibration, respectively.

3.2 Rat study

3.2.1 SO_2 and THb baselines

The tissue physiological parameters were extracted from the FDPM measurements at each time point for each animal using Eqs. (14)–(16). Figure 5 shows boxplots of the baseline SO_2 and THb obtained during carbogen inhalation (8 animals) and forced CH (10 + 4 animals) studies. No significant difference in the baseline THb and SO_2 was found across all the three animal groups indicating that all the animals used for the study had similar baselines in their physiology prior to hyperoxic or hypoxia gas breathing. Slightly raising the O_2 concentration from 21% to 30% didn't significantly change the measured tissue oxygenation showing that the tissue SO_2 isn't very sensitive to a small increase in O_2 from room air.

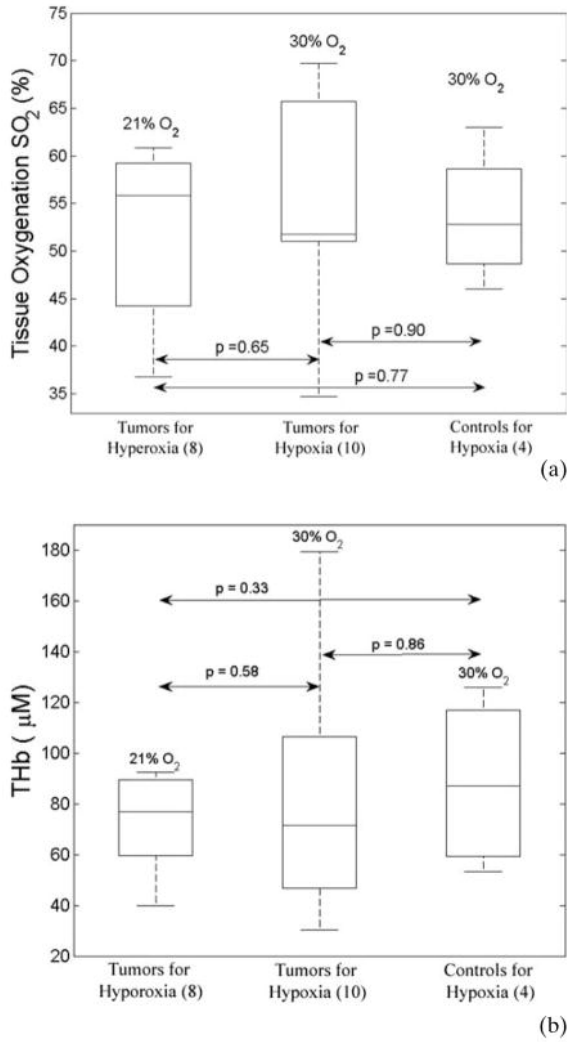

Figure 5 Boxplots of baseline (**a**) SO_2 and (**b**) THb for tumors and controls in the carbogen gas and forced CH studies.

3.2.2 Carbogen inhalation

The physiological responses of a typical rat tumor (Rat #5) to carbogen gas inhalation measured with the side-firing probe are presented in Figure 6. The tumor SO_2 fluctuation was within 4% during the baseline. The mean SO_2 jumped from 58% to 71.5% upon carbogen gas breathing, but did not fully return to the baseline within 20 minutes after being switched back to room air. The fluctuation in THb during the baseline was less than 3 μM. The mean THb dropped from 92.5 to 88.7 μM upon carbogen gas breathing and returned to the baseline within 20 minutes after being switched back to room air. While similar trend for SO_2 has been observed, a slow increase in THb has been recorded in other rats in this group.

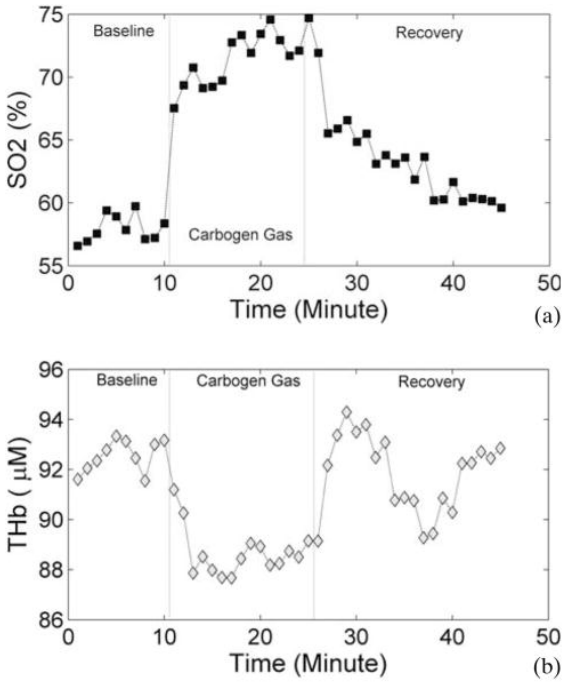

Figure 6 (**a**) SO_2 and (**b**) THb measured from Rat #5 in pre-, during and post carbogen inhalation.

Figure 7 shows the boxplots of changes in SO_2 and THb from the first baseline datapoint (t = 0 minute) for all 8 rats. Significant increase in SO_2 from base-line (p = 3.4e-5) was observed during carbogen inhalation. There was also a significant difference in SO_2 between the baseline and recovery phase (p = 0.01) indicating that SO_2 did not fully return to the base-line during the 20 minutes recovery period. Although there was a small increase in the THb, there was no significant change between the hyperoxia and recovery phases from the baseline (p = 0.74 and 0.12, respectively).

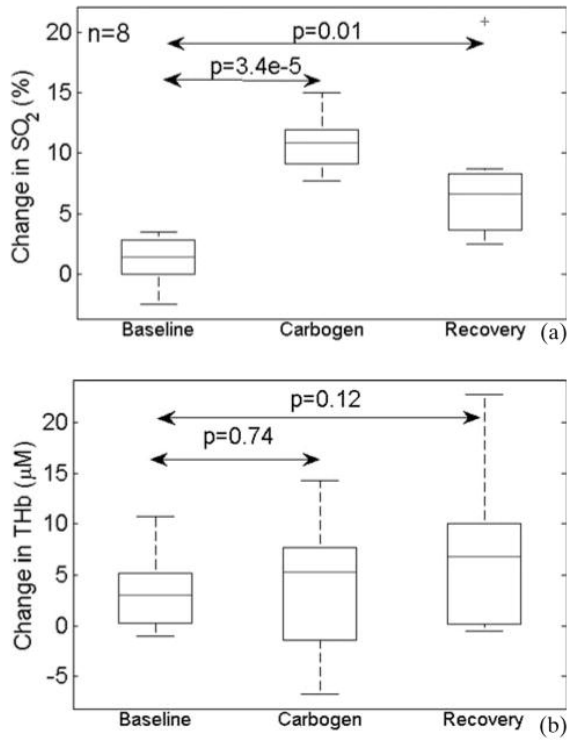

Figure 7 Boxplots of changes in (**a**) SO_2 and (**b**) THb from the first baseline datapoint (*t* = 0 minute) for all 8 rats in the carbogen inhalation study.

3.2.3 Forced CH

The physiological responses of a typical rat tumor (Rat #10) and a normal control (Rat #16) to forced cyclic hypoxia measured with both the side-firing probe and mouse oximeter are shown in Figure 8. The THb for both the tumor and control (Figure 8(a) and (c)) showed a slow increase with some fluctuations through the 50-minute study period, while both the tissue oxygenation measured by the side-firing probe (Figure 8(b)) and arterial blood oxygenation recorded by the MouseOx (Figure 8(d)) followed the cycles of the oxygen supply pattern as shown in Figure 3(b). It is worth noting that the tissue SO_2 is an average over the tissue volume under the side-firing probe which is roughly about 1 cm in diameter and thus is lower than the arterial blood saturation measured with the MouseOx. This is to be expected as there are longitudinal gradients in oxygen when going from the heart to the peripheral arterial circulation as reported by Dewhirst [17]. We also noticed that the response in the tissue oxygenation has a slight delay from that of the arterial blood saturation.

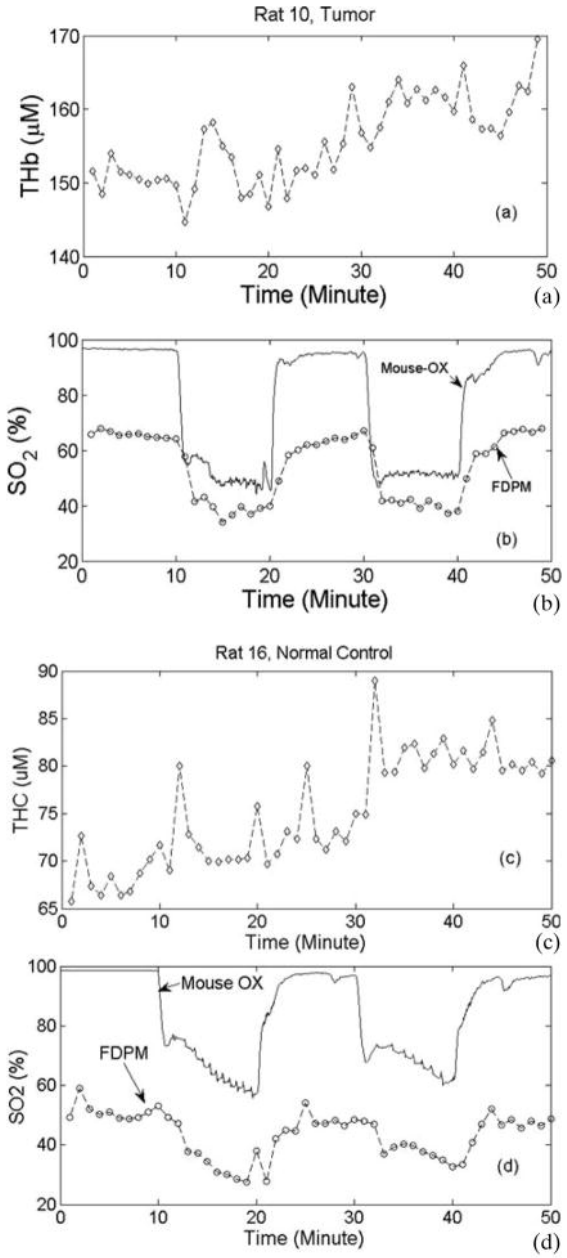

Figure 8 Typical THb and SO_2 measured in the forced CH study from a rat tumor (Rat #10, (**a**) and (**b**)) and a normal control (Rat #16, (**c**) and (**d**)).

Figure 9 shows the boxplots of changes in THb and SO_2 (from t = 0 minute) for normal tissue during normoxia (NN, 4 rats), normal tissue during hypoxia (NH, 4 rats), tumor tissue during normoxia (TN, 10 rats) and tumor tissue during hypoxia (TH, 10 rats). The normoxia (NN and TN) includes all the data points collected during 30% O_2 breathing and the hypoxia (NH and TH) includes all data points measured during 12% O_2 breathing. Significant differences in ΔSO_2 were found between normoxia and hypoxia for both normal (p = 0.024) and tumors (p = 4.2–6) (Figure 9(a)). ΔTHb was significantly higher only for tumors during hypoxia (Figure 9(b)).

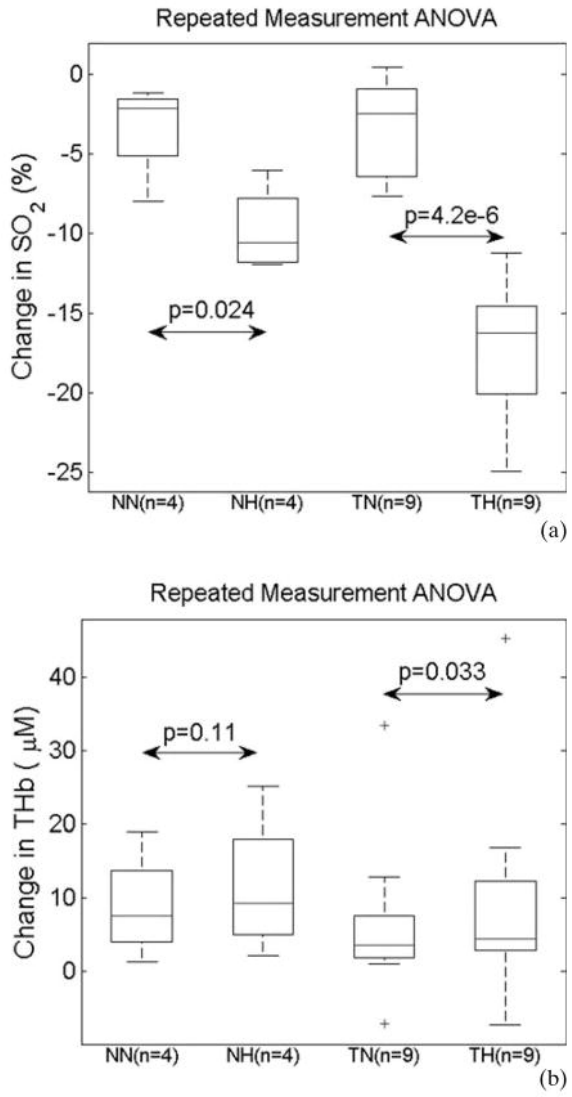

Figure 9 Boxplots of changes (from the 1st data point) in (**a**) SO_2 and (**b**) THb for normal tissue during normoxia (NN), normal tissue during hypoxia (NH), tumor tissue during normoxia (TN) and tumor tissue during hypoxia (TH). The normoxia (NN and TN) includes all the data points collected under 30% O_2 supply and the hypoxia (NH and TH) includes all data points measured under 12% O_2 supply.

3.2.4 Natural CH

A total of 4 rats in Group 3 were used to evaluate the capability of the side-firing probe in capturing natural CH in the tumor. In one of the 2 rats in Group 3A, the probe wasn't in good contact with the tumor surface because the tumor was too stiff. Figure 10(a) shows the tissue oxygenation measured from the other rat in Group 3A on both the right flank muscles and a tumor at a size of 2 cm × 1.7 cm on the left flank. In the normal flank, small fluctuations at a frequency around 2–3 minutes per cycle with a slow increase in the mean tissue SO_2 were recorded. In the opposite flank bearing the FaDu tumor, large fluctuations on top of the small cycles were observed. Similar trend was observed in the concurrently measured THb for both the flank muscles (data not shown in the figures) and and tumor (Figure 10(b). The tumor THb is plotted with SO_2 in Figure 10(b), indicating that tumor oxygenation followed the same trend as total hemoglobin content.

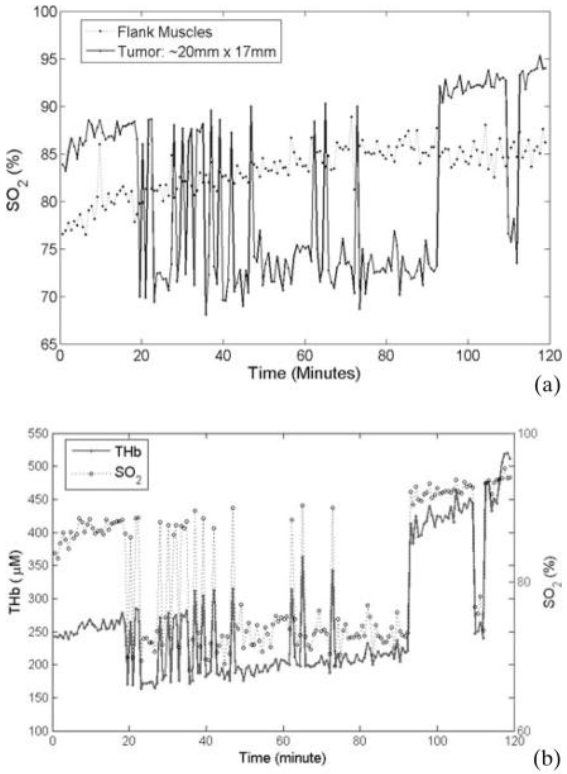

Figure 10 Results measured from the rat in Group 3A: (**a**) Tissue oxygenation measured from the right flank muscles and at a tumor size of 2 cm × 1.7 cm on the left flank; and (**b**) tumor total hemoglobin concentration and oxygenation measured concurrently.

In Group 3B, one of the two tumors grew on the edge of the left flank making it difficult to attach the probe directly on top of the tumor. Figure 11 shows the tissue SO_2 and THb measured from the left flank of the other rat in Group 3B before tumor cells were injected and at three different tumor sizes: invisible (under the skin), 5 mm × 6 mm, and 17 mm × 13 mm. For both tissue parameters, small, but fast fluctuations have been recorded for the muscles (with relatively large slow drifts) and tumor at all sizes, but large and fast amplitude fluctuations were seen only in the 5 mm tumor during the last 50 minutes of the 150 minute measurement period.

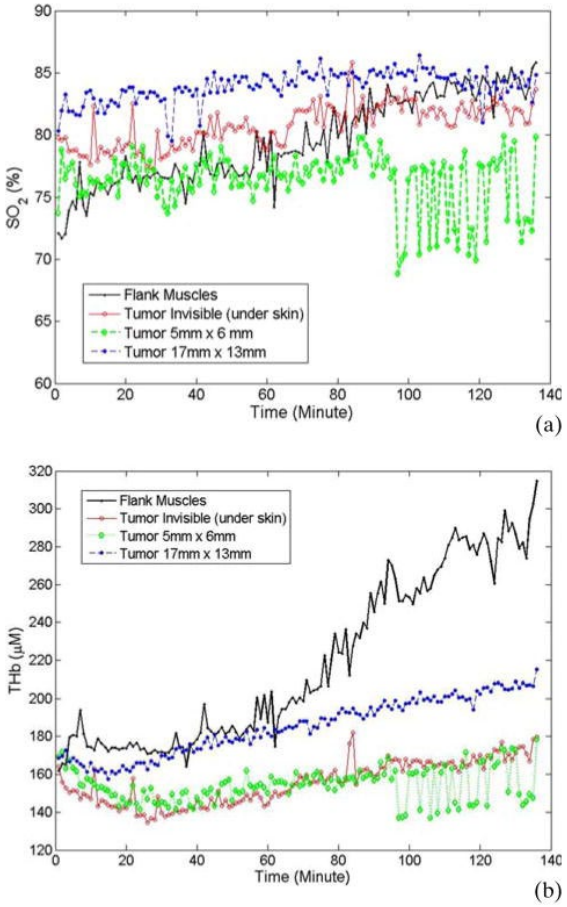

Figure 11 Tissue SO_2 (**a**) and THb (**b**) measured from the rat in Group 3B before tumor cells were injected and at three different tumor sizes.

4. Discussion

Many studies have shown that tumor angiogenesis and hypoxia, particularly CH, can significantly influence the efficacy of radiotherapy and chemotherapy as well as the behavior of surviving cancer cells. Being able to quantify tumor physiological parameters noninvasively and longitudinally has significant value in studying tumor natural variations in the hypoxic profile of the tumor. We have developed a side-firing fiber optic sensor based on frequency-domain photon migration technology that can be used to quantify tissue optical and physiological parameters *in vivo*. The flat design of the side-firing probe makes it easily attachable to any flat surface for longitudinal measurements. We have also developed LabVIEW software that integrates data acquisition and the user interface with a semi-infinite diffusion approximation model in Matlab, which makes it possible to analyze the data and display the physiological parameters in real-time.

The system was validated in a phantom study with 15 tissue-simulating phantoms constructed from Intralipid as scatterer and diluted Indian ink as absorber and the results indicated that the technology can quantify tissue absorption and scattering coefficients with good accuracy. We have compared a frequency-dependent phase offset factor $Z(\lambda, f)$ with a frequency-independent factor $Z(\lambda)$ for phase calibration and found that the former significantly improved the fits between the experimental and modeled phase shift. We also found that a weighting factor α between 0.8–0.9 (vary from phantom to phantom) during the non-linear least square fit slightly improved the fits comparing to equal weight that was used in our previous studies [28] as well as by other groups. The need for larger weight on the amplitude is likely due to the fact that the relative amplitude attenuation is always below 1.0 while the phase shift in degree is often on the order of a few degrees. The

signal-to-noise ratio (SNR) in the amplitude and phase signals could also have played a role in determining the optimal weighting factor α.

The performance of the FDPM system and side-firing sensor was also evaluated for quantification of tissue hemoglobin concentration and oxygenation in pre-clinical studies with 26 athymic nude rats during hyperoxia, forced CH and natural CH.

In all experiments, a small but continuous increase in THb was observed as shown in Figures 7(b), 8(a), 8(c), 9(b), 10(b) and 11(b). There are controversial arguments in the literature on the effects of carbogen gases on tumor THb. There are many investigators who believe that carbogen is vasodilatory – that it could increase blood volume. However, T.J. Dunn et al. found that it was vasoconstrictive [33]. During forced hypoxia, both normal tissue rats and tumors showed raised THb concentration from normoxia as shown in Figure 9b. This is likely due to the increased oxygen deficiency in the animals that has triggered an increase in the blood flow. Probe pressure could also have played a role in modifying the THb concentration by pushing away some of the blood from the areas under the probe when the probe was first taped on the rat skin. This probe pressure released slowly during the course of the experiment allowing some blood to return to the area.

Significant increase in SO_2 upon carbogen inhalation and decrease upon forced hypoxic gas breathing were recorded. Although the increase in tissue SO_2 was quick in both experiments, it took the tumor SO_2 more than 20 minutes to fully recover to the baseline in the carbogen experiment (Figure 7(a)), while both the tumor and normal tissue SO_2 in the forced hypoxia study returned to the baseline (or 30% O_2) within 1–2 minutes (Figure 8(b) and (d)). In another words, the animals can deliver oxygen to hypoxic regions much sooner than they can consume the extra oxygen in the region while there is adequate supply in the blood vessels. The trend of tissue oxygenation for both tumor and normal tissues in the forced CH procedures agree well with that measured with the mouse pulse oximeter from the rat feet, though there was a slightly longer response time in the tissue oxygenation. This time delay is due to the time needed for the oxygen in the arterial blood vessels to reach the microvasculatures in the tumor tissue. The tumors also showed a larger oxygenation change under reduced oxygen supply (from 21% down to 12%) than the normal controls (Figure 9(a)) which can be explained by the fact that normal tissue can regulate the imbalance between oxygen supply and needs more efficiently than a rat with a tumor.

In the two animals breathing room air small fluctuations (less than 5%) in SO_2 were observed with a 2–3 minute period in both flank muscles and tumors (Figures 10(a) and and11).11). Strong fluctuations (over 10%) at a similar frequency in SO_2 were also observed in tumors. Both the patterns and frequencies of the natural CH are very similar to what Braun measured in R3230Ac rat tumors and muscles, using invasive polarographic electrodes [34]. By plotting the tumor total hemoglobin content with the SO_2 measured concurrently from the same tumor (Figure 10(b)), it can be seen that the two parameters followed nearly the same trend. This finding supports the conclusions that natural CH can be attributed to fluctuations in red blood cell flux through a vessel [2, 8, 11, 12]. It was also found that natural CH did not occur in all tumor stages as indicated in Figure 11. More systematic investigation is required to fully understand the characteristics of natural CH and its relationship with tumor growth, metastasis and response to therapy.

Finally, the magnitudes of fluctuations in SO_2 and THb for the tumor in Figure 10 (about 20% and 100 μM roughly) are much larger than that for the tumor in Figure 11 (7% and 20 μM). This difference in SO_2 and THb fluctuations as well as their baseline is attributed to the large heterogeneity both between and within tumor types. Even though Fourier transform analysis in other studies revealed similar kinetics overall, there is still a lot of heterogeneity, even for the same tumor type and tumor size [34–36]. This is likely due to the fact that the underlying biology that causes cycling hypoxia is complex. We believe that it is a reflection of several phenomena, any one of which might be dominant at any time of observation: 1) Arteriolar vasomotion, 2)

rheological changes in hypoxic vasculature that affects how red cells are distributed at bifurcations and 3) vascular remodeling [35–37].

5. Conclusion

The studies reported in this paper demonstrated the ability of the FDPM and side-firing sensor technology to quantify tissue physiological properties noninvasively and in real-time. Because the flat probe can be easily and reliably attached to a tumor surface, it is particularly suitable for monitoring tumor physiological changes at multiple time points per day for a period of several days or even weeks. Although a head and neck tumor model was used in this study for performance evaluation, the technology is readily applicable to the diagnostics and therapeutics for other cancer types.

Acknowledgments

The authors would like to thank Dr. Yulin Zhao for help on preparation of FaDu tumor cell lines for the first experiment and Dr. Thies Schroeder for providing the animal experiment setups for the first two studies. This work was supported by the NIH award R03EB012210, R21CA162747 and CA40355.

References

1. Serganova I, Humm J, Ling C, Blasberg R. *Clin Cancer Res.* 2006;12(18):5260–5264.
2. Dewhirst MW, Cao Y, Moeller B. *Nat Rev Cancer.* 2008;8(6):425–437.
3. Brey EM, King TW, Johnston C, McIntire LV, Reece GP, Patrick CW., Jr *Microvasc Res.* 2002;63(3):279–294.
4. Cao Y, Li CY, Moeller BJ, Yu D, Zhao Y, Dreher MR, Shan S, Dewhirst MW. *Cancer Res.* 2005;65(13):5498–5505.
5. Moeller BJ, Dreher MR, Rabbani ZN, Schroeder T, Cao Y, Li CY, Dewhirst MW. *Cancer Cell.* 2005;8(2):99–110.
6. Liao D, Johnson RS. *Cancer Metastasis Rev.* 2007;26(2):281–290.
7. Toffoli S, Roegiers A, Feron O, Van Steenbrugge M, Ninane N, Raes M, Michiels C. *Angiogenesis.* 2009;12(1):47–67.
8. Cairns RA, Kalliomaki T, Hill RP. *Cancer Res.* 2001;61(24):8903–8908.
9. Cairns RA, Hill RP. *Cancer Res.* 2004;64(6):2054–2061.
10. Dewhirst MW. *Cancer Res.* 2007;67(3):854–855.
11. Toffoli S, Michiels C. *FEBS J.* 2008;275(12):2991–3002.
12. Matsumoto S, Yasui H, Mitchell JB, Krishna MC. *Cancer Res.* 2010;70(24):10019–10023.
13. Vaupel P, Harrison L. *Oncologist.* 2004;9(Suppl 5):4–9.
14. Shweiki D, Itin A, Soffer D, Keshet E. *Nature.* 1992;359(6398):843–845.
15. Dewhirst MW. *Radiat Res.* 2009;172(6):653–665.
16. Intaglietta M, Zweifach BW. *Adv Biol Med Phys.* 1974;15(0):111–159.
17. Dewhirst MW, Ong ET, Rosner GL, Rehmus SW, Shan S, Braun RD, Brizel DM, Secomb TW. *Br J Cancer Suppl.* 1996;27:S241–S246.
18. Ashley HYGMP, Manzoor A, Viglianti Benjamin L, Dewhirst Mark W. *Molecular Imaging: Principle and Practice.* People's Medical Publishing House; USA: 2010. Imaging Hypoxia.
19. Cerussi A, Hsiang D, Shah N, Mehta R, Durkin A, Butler J, Tromberg BJ. *Proc Natl Acad Sci USA.* 2007;104(10):4014–4019.
20. Pham TH, Coquoz O, Fishkin JB, Anderson E, Tromberg BJ. *Review Scientific Instruments.* 2000;71(6):2500–2513.
21. Gulsen G, Birgul O, Unlu MB, Shafiiha R, Nalcioglu O. *Technol Cancer Res Treat.* 2006;5(4):351–363.
22. Shah N, Cerussi AE, Jakubowski D, Hsiang D, Butler J, Tromberg BJ. *Dis Markers.* 2003;19(2–3):95–105.
23. Lee J, Cerussi AE, Saltzman D, Waddington T, Tromberg BJ, Brenner M. *J Biomed Opt.* 2007;12(2):024001.
24. Jakubowski DB, Cerussi AE, Bevilacqua F, Shah N, Hsiang D, Butler J, Tromberg BJ. *J Biomed Opt.* 2004;9(1):230–238.

25. Choe R, Corlu A, Lee K, Durduran T, Konecky SD, Grosicka-Koptyra M, Arridge SR, Czerniecki BJ, Fraker DL, DeMichele A, Chance B, Rosen MA, Yodh AG. *Med Phys.* 2005;32(4):1128–1139.
26. Culver JP, Choe R, Holboke MJ, Zubkov L, Durduran T, Slemp A, Ntziachristos V, Chance B, Yodh AG. *Med Phys.* 2003;30(2):235–247.
27. Pogue B, Testorf M, McBride T, Osterberg U, Paulsen K. *Opt Express.* 1997;1(13):391–403.
28. Yu B, Burnside ES, Sisney GA, Harter JM, Zhu C, Dhalla AH, Ramanujam N. *Opt Express.* 2007;15(12):7335–7350.
29. Fishkin JB, So PTC, Cerussi AE, Gratton E, Fantini S, Franceschini MA. *Appl Opt.* 1995;34(7):1143–1155.
30. Sun Z, Huang Y, Sevick-Muraca EM. *Rev Sci Instr.* 2002;73(2):383–393.
31. Pham TH, Hornung R, Berns MW, Tadir Y, Tromberg BJ. *Photochem Photobiol.* 2001;73(6):669–677.
32. Flock ST, Jacques SL, Wilson BC, Star WM, van Gemert MJ. *Lasers Surg Med.* 1992;12(5):510–519.
33. Dunn TJ, Braun RD, Rhemus WE, Rosner GL, Secomb TW, Tozer GM, Chaplin DJ, Dewhirst MW. *Br J Cancer.* 1999;80(1–2):117–126.
34. Braun RD, Lanzen JL, Dewhirst MW. *Am J Physiol.* 1999;277(2 Pt 2):H551–H568.
35. Cardenas-Navia LI, Mace D, Richardson RA, Wilson DF, Shan S, Dewhirst MW. *Cancer Res.* 2008;68(14):5812–5819.
36. Cardenas-Navia LI, Yu D, Braun RD, Brizel DM, Secomb TW, Dewhirst MW. *Cancer Res.* 2004;64(17):6010–6017.
37. Dewhirst MW, Kimura H, Rehmus SW, Braun RD, Papahadjopoulos D, Hong K, Secomb TW. *Br J Cancer Suppl.* 1996;27:S247–S251.